Programmable Silicon Photonic Optical Thresholder

Chaoran Huang, Thomas Ferreira de Lima, Aashu Jha, Siamak Abbaslou, Alexander N. Tait, Bhavin J. Shastri, and Paul R. Prucnal, *Life Fellow, IEEE*

***Abstract*— We experimentally demonstrate an all-optical programmable thresholder on a silicon photonic circuit. By exploiting the nonlinearities in a resonator-assisted Mach-Zehnder interferometer (MZI), the proposed optical thresholder can discriminate two optical signals with a power contract ratio as low as 1.13. We experimentally achieve a signal contrast enhancement of 40, which leads to a bit error rate (BER) improvement by 5 orders of magnitude and a receiver sensitivity improvement of 11 dB. We present the thresholding function of our device and validate the function with experimental data. Furthermore, we investigate potential device speed improvement by reducing the carrier lifetime.**

***Index Terms*— Optical thresholder, nonlinear silicon photonics.**

I. Introduction

THRESHOLDERS are at the heart of analog-to-digital converters, comparators and operational amplifiers. Thresholders that are based on simple, effective and integrable all-optical components can have operating speeds well beyond the limit of their electronic counterparts. Therefore, all-optical thresholders have found their unique and indispensable role in a variety of applications which require fast signal processing. Examples include neuromorphic photonics, optical code division multiple access (OCDMA), optical logic gate, optical signal regeneration, and physical layer security, etc [1]–[4]. In these applications, all-optical thresholders play a crucial role in effectively enhancing the signal contrast. A poor signal contrast will lead to degradation of the system quality and result in a large bit error rate (BER). An all-optical thresholder can be used to improve the system performance.

Substantial efforts have been made to develop high-performance optical thresholders by exploring different nonlinear effects and materials [2], [5]–[7]. However, most of these systems are constructed with bulky and discrete photonic devices. Recent work [3] demonstrated an integrated, low-power optical thresholder by exploiting Fano resonances on an InP photonic crystal (PhC) membrane structure. This device improved receiver sensitivity by 2 dB.

The development of the silicon-on-insulator (SOI) platforms offers the possibility to integrate optical thresholders on a silicon chip. The high refractive index of silicon enables efficient nonlinear interaction of lights within a short waveguide. Moreover, the nonlinearity of silicon can be further enhanced by cavity structures such as microring resonators (MRRs). Optical thresholders based on silicon MRRs in use with different structures have previously been proposed. However, only numerical simulations have hitherto been shown [8], [9].

In this letter, we propose and demonstrate an all-optical thresholder based on resonator-assisted Mach-Zehnder interferometer (MZI) on a SOI platform, as an extension of our recent conference letter [10]. In addition to signal contrast enhancement demonstration [10], we present the operation principle of our device using a experimentally-validated theoretical model. Using this model, we also characterize the thresholding function and the processing speed of our device. Our thresholder combines of the power-dependent nonlinear phase in the MRR and the high extinction ratio of the MZI, leading to a highly sensitive thresholder with a sharp power transfer slope of 44. With the proposed thresholder, we experimentally demonstrate that two optical signals with very close power levels can be well distinguished, leading to 40 × signal contrast improvement. This consequently leads to a BER improvement by 5 orders of magnitude and a receiver sensitivity improvement of 11 dB.

II. Device Principle, Design and Characterization

The idea of the proposed optical thresholder is to exploit this power-dependent phase shift induced by the nonlinearity in silicon waveguide. In a silicon waveguide, both the Kerr effect and the free carrier dispersion (FCD) can induce a power-dependent phase shift on traveling lights with fast dynamics. It is found that FCD practically dominates over Kerr in the MRR [11]. Therefore, in our current device, FCD is the dominating mechanism that contributes to the nonlinear phase.

In the MRR, near the resonance, the signal experiences a power-dependent nonlinear phase shift that varies rapidly with its optical power. In addition, the MRR can also increase the effective interaction length and instantaneous optical power through coherent power buildup, therefore reducing the required optical power supply. An MZI is used to convert the phase change into an intensity change with a large extinction ratio. With a sufficiently large phase difference, the interference between the signals from the two arms of

Manuscript received May 30, 2019; revised September 29, 2019; accepted October 16, 2019. Date of publication October 22, 2019; date of current version November 20, 2019. This work was supported in part by the Office of Naval Research (ONR) under Award N00014-18-1-2297. *(Corresponding author: Chaoran Huang.)*

C. Huang, T. Ferreira de Lima, A. Jha, S. Abbaslou, and P. R. Prucnal are with the Department of Electrical Engineering, Princeton University, Princeton, NJ 08544 USA (e-mail: chaoranh@princeton.edu).

A. N. Tait is with the Department of Electrical Engineering, Princeton University, Princeton, NJ 08544 USA, and also with the Physical Measurement Laboratory, National Institute of Standards and Technology, Boulder, CO 80305 USA.

B. J. Shastri is with the Department of Electrical Engineering, Princeton University, Princeton, NJ 08544 USA, and also with the Department of Physics, Engineering Physics and Astronomy, Queen's University, Kingston, ON KL7 3N6, Canada.

Color versions of one or more of the figures in this letter are available online at http://ieeexplore.ieee.org.

Digital Object Identifier 10.1109/LPT.2019.2948903

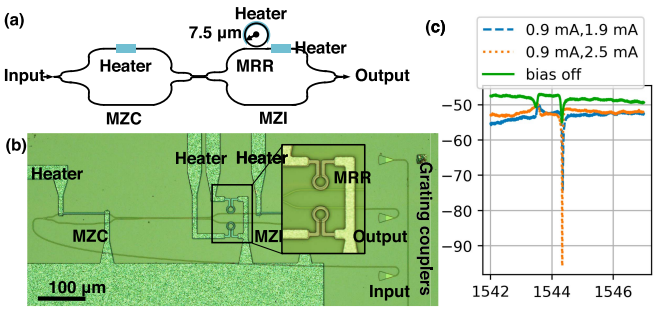

Fig. 1. (a) Schematic illustration of the proposed all-optical thresholder; (b) Microscope image of the fabricated device. The resonance of the MRR on the lower arm of MZI is tuned away from the operating wavelength. (c) Optical spectrum of the device under different biasing current. 0.9 mA is the current at the MZC; 1.9 mA and 2.5 mA are the current at the MZI.

the MZI can switch from constructive to destructive, leading to self-switching. Therefore, we load an MRR in one arm of the MZI, resulting in an all-optical thresholder based on an MRR-assisted MZI (Fig. 1(a)).

To maximize the thresholding effect, it is critical to switch off the low power signal through destructive interference. Perfect destructive interference requires the signals traveling in the two MZI arms to have equal amplitudes and an exact π phase difference. Therefore, we designed a MZC preceding the MRR-assisted MZI through a wideband 3 dB coupler. The bias of the MZC (through the heater) can be adjusted to balance the amplitudes at the two arms of the MZI, while the MZI bias can be independently tuned to introduce a π phase difference. The bias on the MRR also needs to be carefully adjusted to ensure that the thresholder is working around the resonance wavelength to achieve the highest sensitivity.

Our all-optical thresholder consists of fully-etched, 500 nm-wide waveguides (Fig. 1(b)) on a passive-SOI platform with silicon thickness of 220 nm, a 3μm oxide passivation layer, a Ti/W heating filament layer, and an Al routing layer. The MRR on the MZI's arm has a radius of 7.5μm and coupling coefficient is $\sim$0.6% (gap = 100 nm), yielding a Q-factor $\sim$25000. The resonance of the MRR is not used in our experiment. A microheater on the MRR provides flexible resonance control over a full free spectral range (FSR) (18 nm). Thus, input signals of different wavelengths can be easily accommodated. Two microheaters are deposited on the arms of MZC and MZI. These tunable elements can control the interference condition of the device and enable us to locate the sweet spot of thresholding for the signals.

Typical transmission spectra under different microheater DC current biases are shown in Fig. 1(c). When the biases are off (green curve), the resonance features on the transmission spectrum resemble a Lorentzian-like shape with an on-off ratio of $\sim$7.5 dB. When the bias currents are on and optimized (orange curve), the optical power at resonance is $\sim$-90 dBm denoting an off condition. The on-off ratio in this case is found to be more than 45 dB. This result indicates that, the on-off ratio of the MRR can be significantly improved by loading the MRR on the MZI. This highly sensitive transfer function can be explained by the Fano resonance effect, which results from the interference between a resonance pathway (MRR) and a coherent background pathway (MZI) [12], [13]. The minor

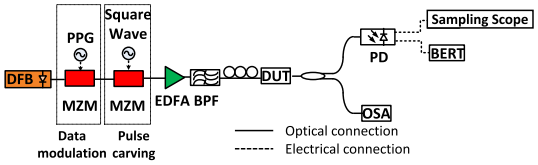

Fig. 2. Experimental Setup: DFB: distributed feedback laser; MZM: Mach-Zehnder; PPG: pulse pattern generation; EDFA: erbium-doped fiber amplifier; BPF: bandpass filter; DUT: device under test; OSA: optical spectrum analyzer; BERT: bit error rate tester.

peak in the transmission spectra is also attributed to the Fano resonance [12].

III. Experiment and Results

The experimental setup is shown in Fig. 2. The signal is generated by modulating a distributed feedback (DFB) laser output using two cascaded MZMs. The first MZM is driven by electrical pulses from a pulse pattern generator (PPG) (Anritsu MP1763b). A pulsed optical signal with $\sim$80 ps pulsewidth and equalized peak power is generated. The second MZM is driven by programed patterns at a data rate of 400Mb/s. This yields a 400Mb/s return-to-zero (RZ) signal with two different power levels, and the contrast between two power levels can be dynamically adjusted by tuning the bias of the second MZM. The data speed is limited by the decay time of the TPA-induced carriers. The optical signal is amplified to 20dBm by an erbium doped fiber amplifier (EDFA) to trigger the nonlinearity in the silicon waveguide and compensate for the fiber-to-chip coupling loss. The optical signal is coupled to the device by free-space coupling through a sub-wavelength grating coupler with $\sim$8 dB coupling loss. The eye diagrams of the input and output signals are obtained by photodetectors and monitored using a sampling oscilloscope (OSC) (Tektronix DSA8300). The signal optical spectrum is monitored using an optical spectral analyzer (OSA) (APEX AP2440A). The microheaters are independently driven by current sources to optimize the parameters to attain a high signal contrast ratio.

Fig. 3(a) shows the device performance using two sets of signals with different input signal contrast ratios (unit-less). Both sets of signals have contrast ratios close to 1, resulting in significantly degraded signal quality (Q-factor (unit-less)) even though the received average powers (0dBm) are much higher than the receiver sensitivity. After being processed by the thresholder, the lower power pulses in both signals are fully suppressed. As a result, the signals after thresholding have a significant signal contrast enhancement ($\sim$40 times for signal 1, and 7.5 times for signal 2), which leads to a Q-factor improvement of 6.4 dB for signal 1 and 8 dB for signal 2. The result confirms that our thresholder works well under signal contrast close to 1.

Fig. 3(b) shows the results of BER measurement of signal 2 using a BER tester (BERT). Assisted with the all-optical thresholder, the communication link can achieve an error-free detection (BER = 10^{-9}) at a received signal power of $-$27.5dBm due to the contrast enhancement leading to an opened eye. Without the thresholder, at the same received power ($-$27.5dBm), the link has a BER higher than 10^{-4}. The presence of this thresholder can also effectively improve the

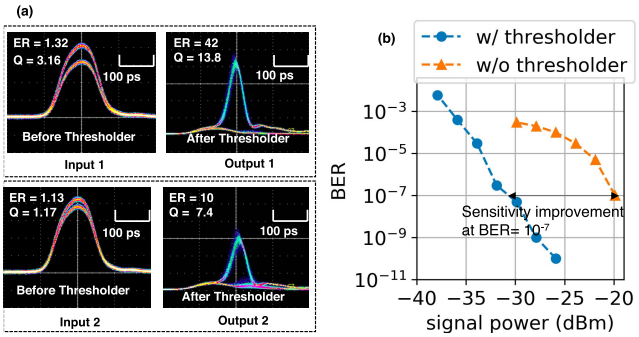

Fig. 3. Eye diagrams of the signals before (left) and after (right) the thresholder for input signal contrast ratios of 1.32 (top) and 1.12 (bottom).

receiver sensitivity by 11 dB at a BER of 10^{-7}(see Fig. 3(b)). The BER performance of the two systems are compared at same received power. The thresholder induces a insertion loss of 8 dB because the operating wavelength is close to the MRR resonance. In considering loss of the thresholder, the receiver sensitivity improvement is 3 dB. However, we would like to point out that the BER performance of low-contrast signals cannot be continuously improved by simply feeding a higher power to the photodetector. The reason is that the photodetector has a saturation input power. Beyond the saturation, the signal contrast will degrade after detection and the eye diagram can be totally closed. In contrast, the optical thresholder can removes the residual 0-level signal, thereby allowing amplification without reaching photodetector saturation. The system performance is evaluated with high signal to noise ratio (SNR). For the low SNR signal, the noise on the 0-level can be suppressed due to the destructive interference while the noise on the 1-level will be amplified. In this case, appropriate biases need to be carefully chosen to minimize the BER.

IV. Thresholding Tranfer Function

To correctly model the thresholding behavior of our device, nonlinearities in the silicon waveguide including the Kerr effect, TPA, TPA induced free-carrier absorption (FCA) and FCD are taken into consideration. Thermal-optic effect is excluded due to its long response time compared to the signal speed. In our simulation model, the MZC and MZI are treated as linear waveguides due to their short lengths. Nonlinear coupled-mode theory is used to study the change in the signal complex amplitude and carrier density in the MRR [14]. The evolution of the normalized complex amplitude a, and the normalized carrier density n is governed by

$$\partial a/\partial t = i(\delta\omega - n_{\text{Kerr}}|a|^2 + \sigma_{\text{fcd}}\alpha_{\text{tpa}}n)a - (1 + \alpha_{\text{tpa}}|a|^2 + \gamma_{\text{fca}}\alpha_{\text{tpa}}n)a + \sqrt{\gamma_p P_{\text{in}}(t)} \quad (1a)$$

$$\partial n/\partial t = |a|^4 - n/\tau, \quad (1b)$$

where $\delta\omega$ is the frequency detuning between the light source and the MRR resonance; t is the time variable normalized with $\Gamma_0^{-1} = 2Q_L/\omega_0$, Q_L is the total quality factor; P_{in} is the power input, and $(n_{\text{Kerr}}, \alpha_{\text{tpa}}, \sigma_{\text{fcd}}, \gamma_{\text{fca}}, \gamma_p) \propto (n_2\omega_0, \beta_2, \sigma_{e,h}\omega_0, \sigma_{\text{fca}}, \Gamma_c/\Gamma_0^3)$, are the Kerr, TPA, FCD, FCA, and quality factor coefficients, respectively. These equations were simplified from Ref. [14], and renormalized so that the two-photon absorption term only appears in Eq. (1a) [11].

The input signals are Gaussian pulses with widths of 100 ps. Their wavelength is located at 150 GHz away from the MRR resonance, and the MRR Q factor is 25000. These conditions are consistent with those in the experimental measurement. The power splitting ratio on MZC and the phase bias on MZI are optimized such that the slope of the transfer function is maximized. The transfer function in Fig. 4(a) shows that, through our thresholder, a signal contrast of 1 dB (the signal contrast is numerically equal to the extinction ratio (ER)of 1.25 between the two input signals is enhanced to 17.4 dB (ER = 54.9) in the output signals, resulting a 44× signal contrast enhancement. Fig. 4(b.i) plots the two input pulses. Fig. 4(b.iii), shows the nonlinearity-induced intensity dependent phase change in the MRR (derived from Eq. 1a), which renders an amplitude shift in the MZI output. Along with this phase change, we can optimize the biases applied to the MZC and MZI to maximize the ratio of the peak powers between two output signals. This can be accomplished when the phase difference of the "1"-level signal and "0"-level signal is approximately π, and a destructive interference occurs on the "0"-level signal while a constructive interference occurs on the "1"-level signal. As a result, the output pulses (shown in Fig. 4(b. iii)) with significantly improved signal contrast are obtained. The output pulse width is determined by the time duration that the signal phase changes from 0 to 2π, which is governed by the nonlinearity in the silicon waveguide. As a result, the output pulse duration has changed after the thresholder. The simulated contrast enhancement and the output pulse width (50 ps) match well with the experimental data. Fig. 4(b.iv) shows the signal phase after the thresholder. Due to the power-dependent nonlinear phase, the output signal experiences a phase distortion. Such a phase distortion can be harmful if the output signal is to be transmitted through an optical fiber with non-negligible dispersion. Therefore, the thresholder should be operated at the receiver end if it is used to process the signals in the fiber communication systems. However, we would like to point out that apart from fiber communication, our thresholder can be applied to other applications such as spiking neural networks, chip interconnect and quantum computing in which the dispersion is negligible.

V. Device Speed Discussion

Although FCD plays a dominant role in discriminating the signals, its long lifetime hinders fast nonlinear signal processing (>10 GHz) in silicon. Therefore, the processing speed of the current device is limited to 400 Mbit/s. A widely applied technique to overcome the speed limitation is by active carrier removal, i.e., reverse-biasing a p-i-n junction transversal to the silicon waveguide to reduce the lifetime of free carriers. The carrier lifetime can be effectively reduced by increasing the reverse-biasing voltage [15].

Here, we study the device speed with active carrier removal and characterize the device speed under different carrier lifetime τ using our simulation model described in Eq. 1a. In device speed characterization, the input signal is an impulse with a pulsewidth <1 ps. The device speed is defined as $1/T$, where T is the time that takes to reduce the free carrier

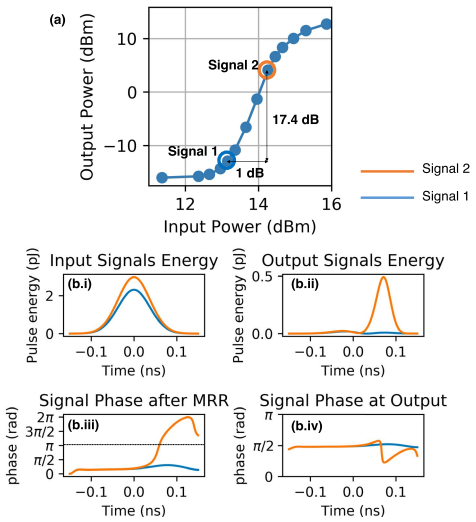

Fig. 4. (a) Power transfer function of the proposed device; (b) Input (i) and output (ii) signal waveforms with two different peak powers; (iii) signal phase evolution, (iv) signal phase at the thresholder output.

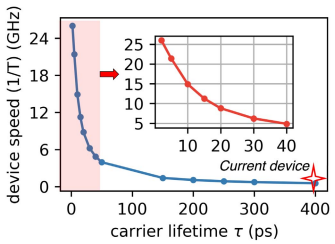

Fig. 5. Device speed as a function of the carrier lifetime; inset: zoom-in view of red region.

number by 99% compared to the peak carrier number. It is worth noting that the definition of T here takes the cavity effect of MRR into consideration, and thus is not equivalent to the carrier lifetime. Fig. 5 shows the device speed as a function of the carrier lifetime. As expected, reducing the carrier lifetime can increase the device speed. With reduced lifetime, the similar thresholding function can still be achieved at the cost of requiring a higher signal power. Our current device operates at a speed of 400 Mbit/s and is marked in Fig. 5. The inset of Fig. 5 is a zoom-in view when the carrier lifetime is smaller than 40 ps. As shown in the inset, our thresholder has the potential of working beyond 10 GHz when the carrier lifetime is reduced to $\sim$ 18 ps [15].

The processing speed limitation imposed by carrier effects can be further relaxed by designing MRR with a lower Q factor. Other alternative approaches include the use of a silicon-organic hybrid waveguide and other TPA-free nonlinear materials [16], [17]. All these methods are compatible with the design of our proposed thresholder.

VI. Conclusion

We have proposed and experimentally demonstrated an all-optical programmable nonlinear thresholder based on resonator-assisted nonlinearity in a Mach-Zehnder interferometer. This device can discriminate signals with extremely close power levels due to its sharp thresholding transfer function. We experimentally demonstrated that this thresholder enables an enhancement of 40 times in signal amplitude contrast, and consequently, an improvement of 11 dB in the receiver sensitivity. The proposed thresholder, developed on a CMOS-compatible silicon-on-insulator (SOI) platform, can find uses in a number of high-performance optical signal processing applications and can be monolithically integrated with other on-chip functionalities. In our future work, we will improve the device design to increase the operation speed and explore other applications using this device.

References

[1] P. R. Prucnal and B. J. Shastri, *Neuromorphic Photonics*. Boca Raton, FL, USA: CRC Press, May 2017.

[2] K. Kravtsov, P. R. Prucnal, and M. M. Bubnov, "Simple nonlinear interferometer-based all-optical thresholder and its applications for optical CDMA," *Opt. Express*, vol. 15, no. 20, pp. 13114–13122, Oct. 2007.

[3] D. A. Bekele *et al.*, "Signal reshaping and noise suppression using photonic crystal Fano structures," *Opt. Express*, vol. 26, no. 15, pp. 19596–19605, Jul. 2018.

[4] C. Huang, P. Y. Ma, B. J. Shastri, P. Mittal, and P. R. Prucnal, "Robustness of optical steganographic communication under coherent detection attack," *IEEE Photon. Technol. Lett.*, vol. 31, no. 4, pp. 327–330, Feb. 15, 2019.

[5] D. Chen *et al.*, "A novel thresholder based on XGM effect in a DFB laser combined with external optical filtering," *IEEE Photon. J.*, vol. 8, no. 1, Feb. 2016, Art. no. 7801307.

[6] T. Hamanaka, X. Wang, N. Wada, and K.-I. Kitayama, "Compound data rate and data-rate-flexible 622 Mb/s–10 Gb/s OCDMA experiments using 511-chip SSFBG and cascaded SHG-DFG-based PPLN waveguide optical thresholder," *IEEE J. Sel. Topics Quantum Electron.*, vol. 13, no. 5, pp. 1516–1521, Sep./Oct. 2007.

[7] J. Zheng *et al.*, "Few-layer phosphorene-decorated microfiber for all-optical thresholding and optical modulation," *Adv. Opt. Mater.*, vol. 5, no. 9, May 2017, Art. no. 1700026.

[8] A. N. Tait, B. J. Shastri, M. P. Fok, M. A. Nahmias, and P. R. Prucnal, "The DREAM: An integrated photonic thresholder," *J. Lightw. Technol.*, vol. 31, no. 8, pp. 1263–1272, Apr. 15, 2013.

[9] H. Kishikawa, T. Kondo, N. Goto, and S. Talabattula, "Optical thresholder consisting of two cascaded Mach–Zehnder interferometers with nonlinear microring resonators," *Proc. SPIE*, vol. 56, no. 8, Aug. 2017, Art. no. 086101.

[10] C. Huang, T. F. de Lima, A. Jha, S. Abbaslou, B. J. Shastri, and P. R. Prucnal, "Giant enhancement in signal contrast using integrated all-optical nonlinear thresholder," in *Proc. Opt. Fiber Commun. Conf. (OFC)*, 2019, pp. 1–3, Paper M3E.2.

[11] T. F. de Lima *et al.*, "Enhancing SOI waveguide nonlinearities via microring resonators," in *Proc. CLEO, Sci. Innov.*, 2019, pp. 1–2, Paper SW3H.7.

[12] L. Zhou and A. W. Poon, "Fano resonance-based electrically reconfigurable add–drop filters in silicon microring resonator-coupled Mach–Zehnder interferometers," *Opt. Lett.*, vol. 32, no. 7, pp. 781–783, Apr. 2007.

[13] M. F. Limonov, M. V. Rybin, A. N. Poddubny, and Y. S. Kivshar, "Fano resonances in photonics," *Nature Photon.*, vol. 11, no. 9, pp. 543–554, Sep. 2017.

[14] S. Chen, L. Zhang, Y. Fei, and T. Cao, "Bistability and self-pulsation phenomena in silicon microring resonators based on nonlinear optical effects," *Opt. Express*, vol. 20, no. 7, pp. 7454–7468, Mar. 2012.

[15] A. C. Turner-Foster *et al.*, "Ultrashort free-carrier lifetime in low-loss silicon nanowaveguides," *Opt. Express*, vol. 18, no. 4, pp. 3582–3591, 2010.

[16] J. Leuthold *et al.*, "Silicon organic hybrid technology—A platform for practical nonlinear optics," *Proc. IEEE*, vol. 97, no. 7, pp. 1304–1316, Jul. 2009.

[17] D. J. Moss, R. Morandotti, A. L. Gaeta, and M. Lipson, "New CMOS-compatible platforms based on silicon nitride and hydex for nonlinear optics," *Nature Photon.*, vol. 7, no. 8, pp. 597–607, Jul. 2013.